Inelastic light scattering by longitudinal acoustic phonons in thin silicon layers: From membranes to silicon-on-insulator structures

J. Groenen,* F. Poinsotte, and A. Zwick
Centre d'Elaboration des Matériaux et d'Etudes Structurales UPR 8011, CNRS-Université Paul Sabatier, 29 Rue Jeanne Marvig, F 31055 Toulouse Cedex 4, France

C. M. Sotomayor Torres
University College Cork, Tyndall National Institute, Lee Maltings, Cork, Ireland;
Catalan Institute of Nanotechnology, Campus de Bellaterra, Edifici CM7, ES 08193 Bellaterra (Barcelona), Spain;
and ICREA-Catalan Institute for Research and Advanced Studies, 08010 Barcelona, Spain

M. Prunnila and J. Ahopelto
VTT Micro and Nanoelectronics, P.O. Box 1000, FI-02044 VTT, Espoo, Finland
(Received 18 July 2007; published 23 January 2008)

We report on inelastic light scattering (ILS) by longitudinal acoustic phonons in thin Si(001) layers (thickness ≈30 nm). Calculations based on the photoelastic model are presented for unsupported and supported layers. We consider ILS by standing longitudinal acoustic modes along [001]. Our calculations take into account the spatial modulations of acoustic, optical, and photoelastic properties. We successively identify their contributions to the scattering efficiency and find that there is a strong interplay between acoustic, optical, and photoelastic cavity effects. The need to consider optical cavity effects is pointed out. It is shown here that they can be included in a convenient way in the scattered electromagnetic fields, by solving the wave equation in the presence of the polarization induced by the photoelastic effect. A detailed analysis of the scattering efficiency (peak frequencies, intensities, and widths) is presented. The dependence of the ILS spectra on film thickness and on substrate characteristics are addressed. Calculations are successfully compared to experimental data for thin Si membranes and silicon-on-insulator structures. It is shown that the inelastic light scattering involves a set of discrete quantized acoustic modes for membranes and a continuum of acoustic modes for silicon-on-insulator structures.

DOI: 10.1103/PhysRevB.77.045420 PACS number(s): 63.22.−m, 78.20.Hp, 78.30.Am

I. INTRODUCTION

Inelastic light scattering (ILS) has proven to be of great value in the study of acoustic excitations and elastic properties of various nm- and μm-sized systems. ILS from supported films and coated surfaces was reported in the late 1970s.[1,2] Since then there has been an undeniable and continuous interest for ILS by acoustic phonons from supported and unsupported films.[3–15] Much interest was devoted to surface and interfacelike excitations. Measurements were performed with Brillouin scattering setups, typically below 40 GHz. Thanks to the high spectral resolution these setups provide, the angular dispersion of the acoustic modes could be investigated in great detail. There are a few reports on Brillouin scattering from unsupported films. In a pioneering experiment by Sandercock, a discrete set of modes, similar to those of open-ended organ pipes, were evidenced for a sub-μm-thick polymer film and μm-thick crystal films.[16] Later, Lamb waves in unsupported 20-nm-thick Au films were investigated as a function of in-plane wave vector.[5] More recently, Brillouin scattering from both longitudinal and transverse standing waves was reported for 100- and 200-nm-thick SiN membranes.[14] Si_3N_4/PMMA double layer membranes were shown to display ILS by longitudinal ones solely.[15] Angular dispersion was measured and mode hybridization between standing and Lamb waves was evidenced.[14,15] Standing wave excitations were observed for supported films by Zhang *et al.* and were found to be similar to the modes of open-ended pipes[12] or closed-end ones.[13] Starting from the theory of Brillouin scattering from surface and bulklike acoustic phonons,[17,18] the theory for supported layers, including elasto-optic and ripple coupling mechanisms, has been progressively developed. A general theory of Brillouin scattering from supported films can be found in Ref. 4. Calculations were successfully compared to experimental data for films with thicknesses in the μm and sub-μm range.[2,3,6,7,13]

To derive quantitative information from ILS experiments, directly comparing spectral features of ILS spectra to acoustic mode characteristics (frequencies, symmetries, density of states,…) is often not sufficient and one has to model the coupling to electrons and the optical effects. Fortunately, some experimental cases allow one to have different degrees of sophistication in the description of the acoustic, optical, and electronic properties. Finding out which description is relevant to a given experimental case is obviously a crucial issue. In this paper we present a detailed study on ILS from thin silicon membranes and silicon-on-insulator (SOI) structures. SOI structures have a Si/SiO_2 bilayer on a silicon substrate. The Si layers investigated here are a few tens of nm thick. ILS by acoustic phonons in silicon-on-insulator (SOI) structures was reported in the mid 1990s, for SOI films with thicknesses in the 150–350 nm range.[8–10] Shear horizontal surface phonons[9] and interface longitudinal acoustic

pseudomodes in the buried silica layers[8,10] were evidenced within the 0–50 GHz range. The corresponding theory was developed in Ref. 19 and angular dispersion and localization of the modes were investigated by comparing experimental and calculated spectra. As dimensions in electronics continuously shrink, one deals with SOI layers having thicknesses of a few tens of nm nowadays. The acoustic mode frequencies which are relevant in ILS go therefore up to the THz range. As a matter of fact, Raman scattering (RS) setups fit well with this spectral range. To the best of our knowledge, there are at least two relevant reports on such thin Si layers. Sotomayor-Torres *et al.* presented ILS by acoustic phonons from a 32-nm-thick silicon membrane in which a discrete set of confined acoustic modes was evidenced.[20] Previously, Balandin reported experimental data from a 30 nm SOI structure and assigned the scattering to a set of confined shear acoustic modes.[21]

The aim of the present paper is to present a detailed and quantitative analysis of the ILS in such thin silicon membranes and SOI structures. We focus on ILS by standing longitudinal acoustic (LA) modes, having displacement fields perpendicular to the layer surfaces, i.e., along the z axis. The spectral range and the type of acoustic modes have not been investigated previously for SOI structures. In this paper we adopt the photoelastic model. This model provides a relevant description of Raman scattering by LA phonons in semiconductor superlattices (SL).[22–29] It was shown to account rather well for thin silicon membrane experimental data.[20] This stimulated us to undertake the study on freestanding and supported thin silicon layers presented here. Photoelastic model ILS calculations and quantum model ones were compared very recently for thin Si membranes.[30] The dependence on optical excitation of electronic transitions was investigated. However, the optical cavity effects, which we will show to be very important throughout the present paper, were not considered in Ref. 30. Optical cavity effects were shown to provide selective enhancement of Raman signals in semiconductor planar microcavities.[31–34] Here, we will consider reflections of incident and scattered fields at the interfaces, within the frame of the photoelastic model. Going beyond the simple comparison between experimental and numerical results, a detailed spectral analysis (including frequencies, intensities, and widths of the spectral features) is provided here. Structures investigated here are stacks of materials having different acoustic, optical, and photoelastic properties. The spectral response of the ILS depends strongly on the corresponding cavities, i.e., the acoustic, optical, and photoelastic ones. We aim to identify their respective contributions to the ILS. Numerical simulations provide a convenient means for pointing out successively the relevant effects. A progressive plan has therefore been adopted, from freestanding membranes to supported layers, and finally, supported bilayers. By comparing ILS from Si layers with and without support we are able to propose reliable assignments. We, e.g., find that the peaks in the ILS spectra from SOI structures are not related to a discrete set of confined modes, as for the Si membrane, but to a continuum of acoustic modes.

The paper is organized as follows. Section II presents briefly the experimental setup used in the inelastic light scattering experiments and details on the samples investigated here. Section III provides a basic theoretical background for the numerical simulations. In Secs. IV and V, we present and discuss calculations for membranes and supported layers, respectively. For both systems, simulations are compared to experimental data. Finally, conclusions are drawn and general trends and implications for future work are discussed in Sec. VI.

II. EXPERIMENTS

A T800 Coderg triple spectrometer equipped with a cooled GaAs photomultiplier was used for the inelastic light scattering measurements. They were performed at room temperature (RT) and the samples were kept in a vacuum in order to avoid air related inelastic light scattering. The 413.1 nm emission of a krypton laser was used for excitation.

The Raman spectrometer setup allows us to investigate the 5–50 cm^{-1} range, which is relevant for the standing acoustic modes in the thin Si layers investigated here (100 GHz=3.3 cm^{-1}). Compared to the Brillouin setups used in the above cited papers, the resolution and rejection is, however, significantly lower. Experimental spectra presented here were recorded with a spectral resolution of $\approx$1.5 cm^{-1}. Due to Rayleigh scattering, the low frequency part of the acoustic range (0–5 cm^{-1}) was not accessible, which is the range the previously cited papers dealing with surface modes were devoted to. Contributions of surface modes in the low frequency range and angular dispersion will thus not be addressed here.

Backscattering (BS) and forward scattering (FS) with incident and scattered wave vectors along the z axis, i.e., perpendicular to the sample surface are considered here. For this scattering geometry, there is no in-plane wave vector transfer $\Delta k_x = k_{i,x} - k_{s,x} = 0$. The $q_x = 0$ acoustic waves, which contribute to the scattering in this geometry, are longitudinal ones, having only displacement fields along the z axis.[35] The ripple mechanism accounts for the ILS by the dynamical corrugation produced by acoustic modes at surfaces and interfaces.[17] We emphasize that the modes we discuss here do not induce such corrugations, thus ripple coupling will not be considered here.

The samples were fabricated on commercially available bonded 100 mm SOI wafers, which are produced by the so-called smart-cut process[36] by SOITEC company. The SOI wafer fabrication process of SOITEC generates some variation to the SOI film thickness. The original thickness showed a long-range variation from roughly 100 nm in the center to about 80 nm at the edge of the wafer, which enabled fabrication of samples with different thickness on a single wafer. The buried oxide (BOX) was 397 nm thick. The sample fabrication started by growth of a 127-nm-thick thermal dry oxide at 1000 °C. This step makes the SOI film thinner by converting roughly 58 nm of Si into SiO_2. Rectangular windows were opened to the oxide on the back side of the wafer by UV lithography and wet etching (the oxidized SOI layer stack in the front was protected by a photoresist). The remaining oxide served as a mask while the Si substrate was

etched down to the BOX layer in 25% tetramethyl ammonium hydroxide (TMAH). At this point we had oxide-Si-BOX layer stacks with and without supporting substrate. Finally, the BOX (in the unsupported regions) and oxide layers were removed in a hydrofluoric acid-water solution. As a result we had Si membranes of an area of $500\times500\ \mu m^2$ and regions with supported SOI.

Calculations are compared to previously reported backscattering (BS) measurements performed on Si membranes.[20] Complementary forward scattering (FS) are presented here as well. The silicon membrane thickness e ranged from 29 to 31.5 nm. Furthermore, we present BS measurements performed on SOI structures, having SOI thicknesses e in the 32–38 nm range and the BOX layer thickness $e_{BOX}=397$ nm.

III. LIGHT SCATTERING BY LA PHONONS

When BS and FS experiments are performed on (001) surfaces, incident and scattered photon wave vectors are along the z axis. As discussed above, we focus on light scattering from LA phonons, having displacements only perpendicular to the (001) layers.[35] The incident and scattered electromagnetic waves and the photoelastically induced polarization to be discussed are polarized in the plane of the layers (x or y axis). Each layer μ within the stack is defined by its mass density ρ_μ, its optical index n_μ, sound velocity v_μ, and photoelastic constant p_μ. The stacking sequence defines the corresponding $\rho(z)$, $n(z)$, $v(z)$, and $p(z)$ profiles. The corresponding elastic constants and acoustic impedances are given by $C_\mu=\rho_\mu v_\mu^2$ and $Z_\mu=\rho_\mu v_\mu$, respectively.

Acoustic modes satisfy boundary conditions, i.e., continuity of the displacement and of the normal stress at the interfaces. We deal with finite or semi-infinite structures: one or two surfaces have to be considered explicitly. The acoustic modes are therefore standing waves. The acoustic cavities are defined by the $\rho(z)$ and $C(z)$ profiles. The displacement field in layer μ has two counterpropagating components: $u_z(\mu,z,t)=(a_\mu e^{iq_z z}+b_\mu e^{-iq_z z})e^{i\omega t}$. The transfer-matrix formalism provides a convenient way to determine a_μ and b_μ (see, for instance, Ref. 39). The acoustic modes carry a strain field, given by a derivative of the displacement field; C_μ connects strain and stress. Note that, according to orthonormalization and second quantization, the displacement fields are proportional to $A_\omega=\sqrt{\hbar/2\omega}$.[37]

We calculate ILS spectra according to the photoelastic model. The photoelastic effect can be described as follows. Acoustic modes cause a modulation in the electronic susceptibility of the medium. In the presence of an incident electric field E_i, the strain due to an acoustic mode $u(z,t)$ induces a polarization given by

$$P_{pe}(z,t)=p(z)\left(\frac{\partial u(z,t)}{\partial z}\right)E_i(z,t). \tag{1}$$

This polarization radiates the inelastic contribution to the scattered light. Hereafter, E_S refers to the scattered field.

Raman scattering by LA phonons in superlattice structures[22,23,25–29] has been investigated according to the photoelastic model. The scattered intensity I is usually calculated according to

$$I(\omega)\propto[n(\omega)+1/2\pm1/2]\left|\int E_i E_s^* p(z)\frac{\partial u}{\partial z}dz\right|^2, \tag{2}$$

where $n(\omega)$ is the Bose-Einstein population factor. The plus and minus signs stand for Stokes and anti-Stokes scattering, respectively. In periodic structures, such as crystals or superlattices, Eq. (2) leads to the usual wave vector conservation law. It was shown to account also for finite size effects in superlattices.[24–28] Confinement of acoustical vibrations in semiconductor planar phonon cavities was evidenced as well, comparing Raman scattering experiments and photoelastic model calculations.[29] When the expression of the electromagnetic fields is known, for instance, in case of propagating electromagnetic waves (infinite SL) or confined ones (optical microcavity), the scattered intensity can be derived easily from Eq. (2). In the present study, we deal neither with simply propagating electromagnetic waves nor fully confined ones. The actual profiles of the incident and scattered fields are determined by the boundary conditions and, therefore, depend on the $n(z)$ and $p(z)$ profiles.

We adopt the following general description to calculate the inelastically scattered electromagnetic field $E_S(z,t)$ driven by $P_{pe}(z,t)$ [Eq. (1)].[38,39] Maxwell's equations lead to the following propagation equation for the scattered electric field when [001] LA modes are involved:

$$\frac{\partial^2 E_S(z,t)}{\partial^2 z}-\frac{n(z)^2}{c^2}\frac{\partial^2 E_S(z,t)}{\partial t^2}=\frac{1}{\epsilon_0 c^2}\frac{\partial^2 P_{pe}(z,t)}{\partial t^2}. \tag{3}$$

This equation fits to our specific scattering geometry and sample orientation. A general formulation, referring to Brillouin scattering with generic scattering geometries and anisotropic materials, can be found in Ref. 4. The general solution $E_S(z,t)$ of Eq. (3) has the two usual contributions, the complementary function (homogeneous part) and the particular integral (inhomogeneous part). The relation between these two parts depends on the geometrical details of the scattering experiment and sample.[38] Indeed, to solve this differential equation one needs to consider the appropriate boundary conditions for the electromagnetic fields at the interfaces. As reflections occur at each interface, the general form of the electromagnetic fields has counterpropagating components. The scattered fields E_S are calculated according to the transfer-matrix method presented by He, Djafari-Rouhani, and Sapriel,[39] which included spatial modulations of the elastic, photoelastic, and optical properties in the photoelastic model calculation of ILS by LA phonons in infinite SL.[39] Finally, the intensity of the scattered field is obtained by forming $|E_S|^2$.

Calculated spectra have been convoluted with a Gaussian function (full width at half maximum Γ), to simulate the broadening due to the experimental spectral resolution. Calculations will be compared to experimental data from Si membranes and SOI layers. The relevant numerical parameters are $C_{Si}=166$ GPa, $\rho_{Si}=2.33$ g cm^{-3}, $C_{SiO_2}=78.5$ GPa, $\rho_{SiO_2}=2.20$ g cm^{-3}.[9,40] The corresponding sound velocities are $v_{Si}=8430$ m s^{-1} and $v_{SiO_2}=5970$ m s^{-1}. At $\lambda_i=413.1$ nm,

the optical indexes are $n_{Si}=5.222+i0.269$ and $n_{SiO_2}=1.46$.[41,42] The photoelastic coefficient is taken to be a function of position z. This approach has been widely used in superlattice studies[22,23,25–29] and was shown to yield relevant descriptions far from resonances with electronic transitions. Here the photoelastic effect is supposed to occur in the silicon material only. For the excitation wavelength we used, $\lambda_i=413.1$ nm, it is reasonable to disregard contributions from SiO_2 since in the visible range, $p_{Si} \gg p_{SiO_2}$.[9] Close to electronic transitions, p has complex values.[43] At $\lambda_i=413.1$ nm, the imaginary part is much smaller than the real one for Si. For the sake of simplicity, we assume p_{Si} to be real and constant within the Si layer.

IV. MEMBRANES

In this section we present inelastic light scattering from membranes. We first briefly recall some basic results concerning acoustic modes in membranes. Thereafter we successively point out the role of the scattering geometry and the optical cavity effects. Finally, calculations and experimental data are compared.

A. Acoustic modes

A freestanding membrane corresponds to a very simple acoustic cavity geometry. The LA modes, having displacements perpendicular to the membrane surfaces, are similar to those of open-ended organ pipes. Due to the stress-free boundary conditions imposed at the lower and upper membrane surfaces, eigenmodes are quantized in wave vector, according to

$$q_m = \pi m/e, \tag{4}$$

e being the membrane thickness and the mode index m being an integer. Within the linear dispersion regime of acoustic modes, eigenmodes are regularly spaced in frequency, according to $\omega_m=vq_m$ and Eq. (4). The discrete set of eigenfrequencies is shown in Fig. 1 for a 30-nm-thick Si membrane: $\pi v/e=4.6$ cm^{-1}. The corresponding eigenmodes are standing waves confined within the membrane, their displacement fields being given by

$$u_m(z) = A_m[e^{iq_m z} + (-1)^m e^{-iq_m z}], \tag{5}$$

where $A_m=\sqrt{\hbar/2\rho V\omega}$ (V is the membrane volume). The origin of the z axis is chosen to be located at the middle of the membrane. m indicates the number of nodes in the displacement field. With respect to the center, even (odd) m values yield symmetric (antisymmetric) displacement fields. The insets in Fig. 1 show $u_1(z)$ and $u_2(z)$ and their derivatives.

B. Scattering geometry

When membranes are thin enough to allow light to go through, it is essential to consider both BS and FS. As will be shown below, optical cavity effects play a major role in the scattering efficiency. However, we shall first discard electromagnetic wave reflections at the membrane surfaces. Assuming propagating incident and scattered fields ($E_i=e^{i(k_i z-\omega_i t)}$ and $E_s=e^{i(k_s z-\omega_S t)}$), Eq. (2) provides the following expression for the scattered intensity (Stokes component):

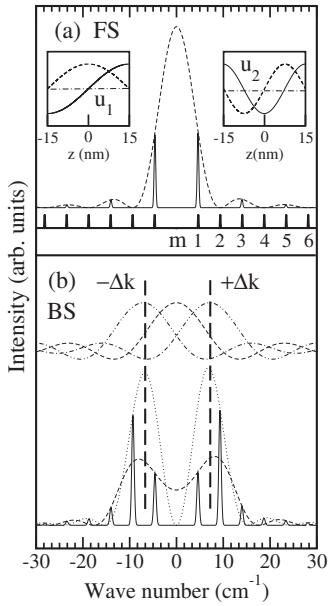

FIG. 1. Calculated spectra of a 30 nm Si membrane (RT and $\lambda_i=413.1$ nm): (a) FS spectrum and envelope (solid and dashed lines, respectively). Eigenmode frequencies are indicated as a function of mode index m. Insets show the $u_1(z)$ and $u_2(z)$ displacement fields and their derivatives (solid and dashed lines, respectively). (b) BS spectrum, odd and even mode intensity envelopes (solid, dashed, and dotted lines, respectively). $\mathrm{sinc}(q_m e/2)$, $\mathrm{sinc}[(2k_i \pm q_m)e/2]$ functions (dashed and dot-dashed lines, respectively). Vertical dashed lines indicate the bulk Brillouin frequency $\pm\Delta k$.

$$I(q_m) \propto [n(q_m)+1]A_m^2 q_m^2(\mathrm{sinc}[(k_i-k_s+q_m)e/2] - (-1)^m \mathrm{sinc}[(k_i-k_s-q_m)e/2])^2. \tag{6}$$

The cardinal sinus $\mathrm{sinc}(Q)=\sin(Q)/Q$ is related to the Fourier transform of the photoelastic constant profile $p(z)$ [Eq. (2)]. Obviously, this is similar to light diffraction by a slit having a rectangular aperture function in wave optics. Equation (2) contains two sinc terms because we considered coupling to standing modes u_m, having two counterpropagating parts [Eq. (5)].

The exchanged photon wave vector $\Delta k=k_i-k_s$ depends on the scattering geometry. Within the simple scheme of plane wave incident and scattered fields (corresponding to the bulk case), $\Delta k \approx 0$ in forward scattering (FS) and $\Delta k \approx 2k_i$ in backscattering (BS).

For FS, Eq. (6) reads

$$I(q_m) \propto [n(q_m)+1]A_m^2 q_m^2 \,\mathrm{sinc}^2(m\pi/2)[1-(-1)^m]^2. \tag{7}$$

When $\Delta k=0$ (FS), the intensity of a given mode u_m is simply given by the integral of $\partial u_m/\partial z$ [Eq. (2)]. Thus, only odd modes contribute to the FS spectrum reported in Fig. 1(a).

Figure 1(b) shows that both odd and even modes do contribute to the BS. At first sight a rather complex intensity modulation is observed, in contrast with the monotonic de-

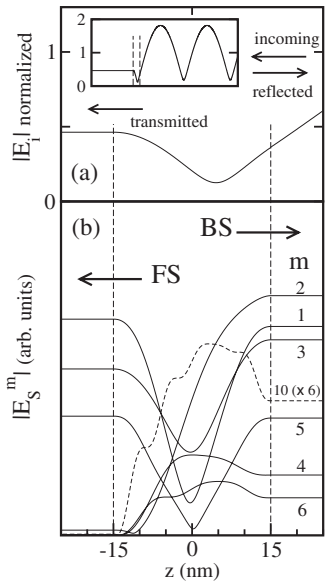

FIG. 2. (a) Modulus of the incident electric field $|E_i(z)|$. $|E_i(z)|$ is normalized to the incoming component. The incoming laser beam is partially reflected and transmitted. The inset shows a larger scale plot. Vertical dashed lines indicate the membrane surfaces. (b) Modulus of the scattered field $|E_S^m(z)|$. $|E_S^m(z)|$ is collected on both sides of the membrane, according to the BS and FS configurations.

cay of FS. Indeed, unlike for FS, one cannot identify a single envelope function for the scattered intensity.

For BS, the envelope for the odd modes, ξ_{odd}, is proportional to

$$(\mathrm{sinc}[(\Delta k + q_m)e/2] + \mathrm{sinc}[(\Delta k - q_m)e/2])^2,$$

and the one for the even modes, ξ_{even}, is proportional to

$$(\mathrm{sinc}[(\Delta k + q_m)e/2] - \mathrm{sinc}[(\Delta k - q_m)e/2])^2.$$

Both ξ_{even} and ξ_{odd} contain two sinc functions. With respect to zero, the latter are shifted by $\pm\Delta k$ [see Fig. 1(b)]. These shifts do correspond to the bulk Brillouin frequency $q=\Delta k \simeq 2n/\lambda_i$. When these sinc functions have the same sign (opposite signs), $\xi_{even} > \xi_{odd}$ ($\xi_{even} < \xi_{odd}$). The resulting oscillations in ξ_{even} and ξ_{odd} account for the BS intensity modulation reported in Fig. 1. This modulation depends strongly on Δk, i.e., on the optical index and wavelength.

C. Optical cavity effects

Considering propagating electromagnetic waves (Sec. IV B) is equivalent to having two different and independent internal scattering geometries, i.e., internal FS and BS. We actually deal with a silicon membrane in air or vacuum, i.e., media with significantly different optical indexes. Thus, one needs to go beyond the simple picture used above and consider optical cavities explicitly. At both the air and membrane interfaces, electromagnetic waves are partially reflected and transmitted.

Figure 2(a) shows the modulus of the incident electric field $|E_i(z)|$. The laser field used is partially transmitted and reflected. The inset in Fig. 2(a) shows that for $z > 15$ nm a

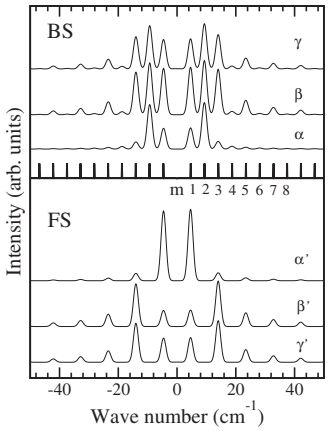

FIG. 3. Calculated spectra of a 30-nm-thick Si membrane (RT, $\lambda_i=413.1$ nm, $\Gamma=1.2$ cm^{-1}). α, β, and γ (α', β', and γ') are BS (FS) spectra. Calculations without optical cavity effects (α and α'), with optical cavity effects (β and β') and with optical cavity effects and optical absorption (γ and γ'). Eigenmode frequencies are indicated as a function of m.

standing wave has formed, resulting from the superposition of incident and reflected components. The transmitted component ($z < -15$ nm) displays a constant modulus, corresponding to the wave propagating away from the membrane. Within the membrane, $|E_i(z)|$ has two counterpropagating components. $|E_i(z)|$ is not constant within the 30 nm Si membrane. Obviously, $|E_i(z)|$ introduces a striking asymmetry.

We are actually interested in the scattered fields outside the membrane, i.e., external FS and BS. The scattered fields can be derived from Eq. (3), provided that boundary conditions and the $n(z)$ and $p(z)$ profile are considered. Figure 2(b) shows the modulus of the scattered electric field $|E_S^m(z)|$ for several acoustic mode orders m.

Inside the membrane, the $|E_S^m(z)|$ profiles correspond to standing waves; they are far from being uniform and depend much on the parity of m. $|E_S^m(z)|$ display thus a clear signature of the $P_{pe}(z,t)$ polarization related contribution [via the particular solution in Eq. (3)]. Indeed, $P_{pe}(z)$ is proportional to the strain field and the incident electric field [Eq. (1)]. Even (odd) m modes have antisymmetric (symmetric) strain fields. $P_{pe}(z)$ has a spatial dependence given by the phonon wavelength $\lambda_m=2e/m$. The resulting modulations in $|E_S^m(z)|$ can be easily seen in Fig. 2(b) for high mode orders. $|E_S^{m=10}(z)|$ was included, in order to provide a clear example.

Acoustic and electromagnetic boundary conditions determine the actual $|E_S^m(z)|$ profiles inside and outside the membrane. On both sides of the membrane, $|E_S^m|$ has constant values, corresponding to the amplitudes of waves propagating away from the membrane. The external values of $|E_S^m(z)|$ define the FS and BS contributions of each acoustic mode m, considering that the scattered intensity is given by $|E_S^m|^2$. The way scattered light gets out on each side of the membrane is ruled by the acoustic and electromagnetic boundary conditions.

Figure 3 shows the corresponding BS and FS spectra, which include the optical cavity effects. Calculations performed with and without optical absorption are rather simi-

lar; optical absorption at λ_i=413 nm yields small changes in the relative peak intensities. In order to evidence the optical cavity effects, the spectra previously shown in Fig. 1 are reported again, for comparison. Obviously, including optical cavity effects has a major impact on both the BS and FS spectra. The main features can be summarized as follows: For FS, the strongest contribution arises from the $m=3$ mode, instead of from the $m=1$ one. For BS the $m=1$, 2, and 3 modes have strong and comparable contributions. At higher mode orders, the BS spectrum displays a series of alternating weak and medium peaks.

Optical field reflections at the top and bottom membrane surfaces have a major impact on the actual electric field profiles inside the membrane (Fig. 2) and external BS and FS efficiencies (Fig. 3). Specific contributions of reflected beams were reported previously by Jusserand *et al.*[45] for Raman scattering by acoustic phonons in freestanding SLs. Internal reflections of optical fields at the surface of the freestanding SL were shown to enable FS (BS) related features to be observed in BS (FS) geometries.[45] In an optical microcavity structure, photons are multiply reflected due to the Bragg mirrors, leading to FS events in addition to the normal BS ones.[27,29,31,33] Internal FS- and BS-like components were identified in the Raman efficiency of semiconductor planar microcavity structures. Interference effects, resulting from the coherent addition of the internal FS and BS components, were evidenced by Trigo *et al.*[27,29] The same scheme can be adopted to analyze our membrane data. Indeed, the external optical field components we calculated (Fig. 2) are related to the internal ones, according to the boundary conditions to fulfill. The external BS and FS efficiencies can therefore be discussed as resulting from the coherent superposition of internal BS and FS electric field components. The resulting interferences account for the significant changes observed, when comparing the spectra calculated with and without optical cavity effects in Fig. 3. For instance, the $m=1$ contribution is lowered in FS and enhanced in BS, indicating destructive and constructive interferences, respectively. This explicitly shows that the actual intensity modulation in both BS and FS depend strongly on the continuities of the incident and scattered optical fields at the surfaces.

Thus depending on e and λ_i, rather different intensity modulations are expected. Figure 4 shows how the BS scattering efficiency changes when increasing e from the thin membrane spectra discussed above to the thick membrane ones. For the thick membranes, the effect of reflection of the incident optical field at the back side of the membrane is limited by the optical absorption however. Consequently, for the $e=1$ μm membrane, only the bulklike BS peak centered at $q_z=\Delta k$ is observed. For thin membranes, internal BS and FS components effectively interfere because they have a significant spectral overlap. This overlap depends on the width at the base of their envelopes (see Fig. 1). The BS component being centered at $q_z=\Delta k$, this overlap disappears when e increases. As a matter of fact one can clearly identify the FS and BS contributions in the $e=150$ nm spectrum. The BS component displays the triplet feature discussed in Ref. 16. Whereas it involves high order modes for thick membranes, it involves the three lowest order modes for the thin Si membranes investigated here. The spectral resolution determines

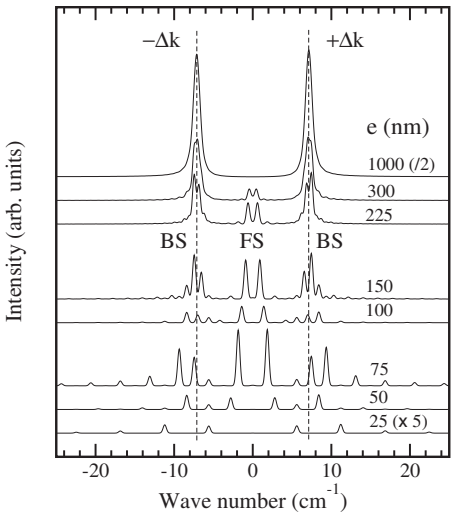

FIG. 4. Calculated BS spectra of Si membranes (RT, λ_i =413.1 nm and Γ=0.5 cm^{-1}). Vertical dashed lines indicate the bulk Brillouin frequency $\pm\Delta k$. BS and FS refer to internal backscattering and forward scattering components.

up to which thickness individual contributions of mode are resolved. Light absorption contributes also to the peak width. For thick and strongly absorbing membranes, peaks will clearly involve a continuum of modes, similar to absorbing semi-infinite systems. Figure 4 shows that the interferences between internal BS and FS components play a specific role for the thin membranes we investigate here.

D. Comparison with experiment

The full calculation including optical cavity effects provides the external BS and FS scattering efficiencies relevant for comparison with experiment. Figure 5 shows experimental spectra from a 31.5-nm-thick silicon membrane together with a numerical solution of Eq. (3). Calculated spectra fit rather well to the experimental data. As expected, only odd order modes contribute to the FS spectrum. The BS spectrum displays two strong peaks, corresponding to the $m=2$ and 3 modes which fit within the main maxima of the envelopes. The Rayleigh scattering hinders the observation of the contributions of the $m=1$ mode (see also Ref. 20). Higher order mode contributions in the BS spectrum up to $m=7$ are also observed. The weak peaks expected for the high even order modes ($m>2$) are not evidenced. The intensities of the high odd order modes ($m>3$) seem to be slightly overestimated in the calculations.

Peak positions are given by the sound velocity and membrane thickness, i.e., by the acoustic cavity. The left inset in Fig. 5 shows data from a series of membranes with e ranging from 28 to 32 nm. Data scale linearly with m/e as expected [Eq. (4)]. Because the intensity decreases rapidly with increasing mode order, one can only measure the approximate frequencies of high order modes. One should note that the width of the peaks is about the experimental resolution, which was determined by measuring the Rayleigh scattering peak.

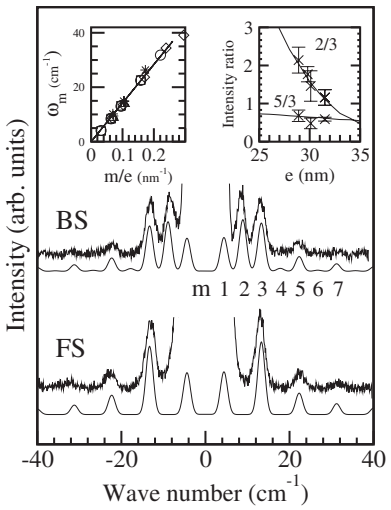

FIG. 5. Experimental and calculated FS and BS spectra of a 31.5-nm-thick silicon membrane (RT, λ_i=413.1 nm and Γ =1.8 cm^{-1}). Left inset: experimental peak positions ω_m versus m/e for a series of membrane with e ranging from 29 to 31.5 nm (each symbol corresponds to a given value of e). The theoretical linear dependence is reported as a solid line. Right inset: Calculated (solid lines) and experimental (symbols) $I_{m=2}/I_{m=3}$ and $2\times I_{m=5}/I_{m=3}$ BS intensity ratios versus e (labeled 2/3 and 5/3).

The simulations account for the ratio between peak intensities within a given spectrum, for both FS and BS. As the relative intensities are determined by the optical and photoelastic cavity effects, they depend on the membrane thickness. $I_{m=3}/I_{m=2}$ and $2\times I_{m=5}/I_{m=2}$ intensity ratios are reported versus e in the right inset in Fig. 5: $I_{m=3}/I_{m=2}$ decreases rapidly with increasing e. Again a good agreement between experiment and simulation is obtained.

To conclude this part, we emphasize that the membrane spectra correspond to contributions of a discrete set of acoustic modes, i.e., the longitudinal acoustic confined modes. The peak positions are therefore determined solely by the acoustic cavity. Three different cavities have to be considered in order to account quantitatively for the intensities:

(i) An acoustic cavity, which determines the frequencies and amplitudes of the eigenmodes.

(ii) A photoelastic one, resulting from the $p(z)$ photoelastic profile, which determines the spectral extent or envelope of the scattering efficiency.

(iii) An optical one, resulting from the refractive index contrast, which implies reflections of the electromagnetic fields at the interfaces and interferences between internal scattering geometries.

There is a strong interplay between these cavity effects when calculating the scattering efficiency. Calculating scattered intensities provides a valuable insight on the spectral behavior. In previous reports on membranes,[5,14–16] experimental spectra were analyzed in terms of acoustic mode dispersion and displacements, but none were compared to calculated spectra. Performing both FS and BS allows one to probe optical cavity effects.

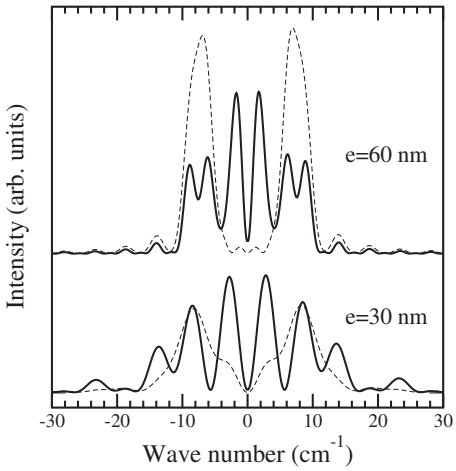

FIG. 6. Calculated BS spectra of supported Si layers (e=30 and 60 nm) acoustically matched to their substrate, with and without optical mismatch (solid and dashed lines, respectively). RT, λ_i =413.1 nm and Γ=0.6 cm^{-1}.

V. SUPPORTED LAYERS

We now consider thin supported silicon layers. Unlike for membranes, a continuum of acoustic modes is available.[44] Numerical results dealing with thin silicon layers on substrates will be presented first. Calculations will be compared thereafter to experimental data on SOI structures. In this section, we assume that the photoelastic effect occurs in the silicon layer(s) only. Note that, as we deal with thick absorbing substrates, only BS is considered from now on.

A. Supported Si

1. Photoelastic and optical effects

We first discuss scattering from a 30 nm silicon layer which is acoustically matched to its substrate. When $Z_{\mathrm{Si}}=Z_{sub}$, acoustic waves are not reflected at the Si/substrate interface. From the previous section, we know that both the photoelastic and optical cavities contribute to the spectral dependence of the scattering efficiency. In order to identify the photoelastic contribution, one may assume to have no optical mismatch, i.e., no electromagnetic wave reflections, at the Si/substrate interface in the calculations. BS spectra were calculated according to Eq. (3), without and with optical mismatch at the lower interface (we took $n_{sub}=n_{\mathrm{Si}}$ and $n_{sub}=n_{\mathrm{SiO_2}}$, respectively). They are reported in Fig. 6 for e =30 and 60 nm.

Spectra calculated without optical mismatch display broad bands, corresponding to the activation of the continuum of LA modes. The spectral extent and modulation are directly related to the $p(z)$ profile, i.e., constant within the Si layer and zero in the substrate. The modulation period scales inversely with the layer thickness e. Taking into account electromagnetic wave reflections at the Si/substrate interface modifies significantly the spectra. Weak features and shoulders in the broad bands transform into sharp peaks. For instance, the intensity of the first peak is strongly enhanced, as seen at $\approx$2 and 4 cm^{-1} for e=60 and 30 nm, respectively.

Electromagnetic wave reflections at the Si/substrate interface imply the superposition of internal FS and BS configurations. The resulting interferences account for the relative enhancement or decrease of intensity one observes when comparing spectra calculated with and without optical mismatch. This behavior is similar to what was discussed in Sec. IV (see Fig. 2). Clearly, there is a major difference among membranes and supported layers since the former ones involve a set of discrete modes and the latter a continuum of modes. As a matter of fact, in contrast with the membrane case, the width of the peaks in the supported layer spectra have an intrinsic contribution in addition to the spectral resolution. This intrinsic width is directly related to the $p(z)$ profile and layer thickness.

2. Acoustic effects

Here we aim to investigate how the scattering efficiency depends on the acoustic cavity effects. We therefore varied the acoustic mismatch between the Si layer and substrate (defined by $\Delta = Z_{sub}/Z_{Si} - 1$). Negative (positive) Δ values correspond to soft (hard) substrates. Optical mismatch was included in the calculations (we considered $n_{sub} = n_{SiO_2}$).

Figure 7(a) shows how the amplitude of acoustic modes in a 30-nm-thick supported silicon layer depends on wave number, for several acoustic mismatches Δ. Whatever the mismatch, a continuum of acoustic modes is available. For the acoustically matched layer ($\Delta = 0$), the amplitude of the modes scales like $1/\sqrt{\omega}$, according to the acoustic mode normalization. For mismatched layers, resonances in the vibrational amplitude occur. The larger the mismatch, the sharper and stronger the acoustic resonances are. Whatever the negative mismatch, acoustic resonances appear for the same wave vectors (wave numbers) given by $q_m = m\pi/e$, corresponding to the wave vector quantization of the free membrane [Eq. (4)]. As a matter of fact, for a vanishing substrate density ($\Delta \to -1$), the free membrane configuration and its frequencies are recovered. For positive mismatches, acoustic resonances appear for another fixed set of frequencies. For large positive Δ values (for instance, 14.2 in Fig. 7), one almost reaches the limit of a rigid substrate. The corresponding boundary conditions for the silicon layer are a free upper surface and a clamped lower surface: they yield acoustic resonances at $q_m = (m+1/2)\pi/e$; with respect to $\Delta < 0$, they are shifted by a half period. Acoustic resonances have an intrinsic width. Even for the limiting cases shown here ($\Delta = -0.97$ and 14.2) finite acoustic resonance widths are obtained.

Figure 7(b) shows some selected displacement fields for $\Delta = -0.97$, 0, and 14.2. Modes are shown for three frequencies, 9.4, 7, and 8.2 cm^{-1}, belonging to acoustic resonances of the $\Delta < 0$ and $\Delta > 0$ series, and being in-between, respectively. For $\Delta = -0.97$, apart from the frequencies close to acoustic resonances the amplitude of the acoustic mode in the silicon layer vanishes. At resonance the displacement field inside the silicon layer is akin to the one discussed previously for the freestanding membrane (see u_2 in Fig. 1). We emphasize that this mode is, however, not confined within the silicon layer since it has a similar amplitude in the substrate. For large positive Δ, the vibrational amplitude in the Si layer becomes very large at resonance, compared to the one in the substrate, whereas off resonance, displacements are weak.

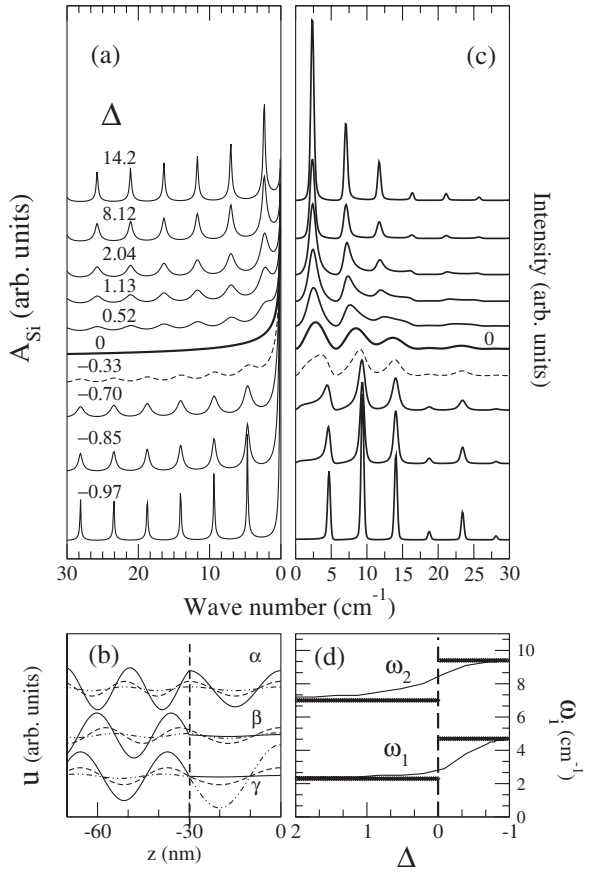

FIG. 7. Data calculated for a 30-nm-thick Si supported layer as a function of the acoustical mismatch Δ: (a) $A_{Si}(\omega)$ amplitudes of the acoustic modes in the Si layer. $\Delta = -0.33$ (dashed curve) corresponds to Si on SiO_2. (b) Selected displacement fields $u(z)$. α, β, γ correspond to 9.4, 8.2, and 7 cm^{-1}, respectively. Solid, dashed, and dot-dashed lines correspond to $\Delta = -0.97$, 0, and 14.2, respectively. The vertical line indicates the position of the substrate/layer interface. (c) BS spectra (RT, $\lambda = 413.1$ nm and $\Gamma = 0.5$ cm^{-1}). (d) Calculated frequencies of the two first peaks, ω_1 and ω_2, versus Δ. Horizontal lines indicate the acoustic resonance frequencies. $\Delta = -0.33$ corresponds to the SiO_2 substrate.

Figure 7(c) shows the corresponding calculated spectra [Eq. (3)]. The acoustically matched layer spectrum $\Delta = 0$ is our reference, as it includes the optical and photoelastic effects only. Significant changes occur as a function of Δ. A convenient way to explain these changes is to consider that the acoustic resonances reported in the left panel act as multiple bandpass filters on spectrum $\Delta = 0$. When the acoustic resonance widths get narrow, these acoustic resonances impose the peak positions and widths, as in the case for the top and bottom spectra in Fig. 7(c) with $\Delta = 14.2$ and -0.97, respectively. Explaining the scattering efficiency is mainly a matter of evaluating to what extent the acoustic resonances fit with the maxima in spectrum $\Delta = 0$. For $\Delta < 0$, the second and third resonances fit actually better to maxima in the $\Delta = 0$ spectrum, than the first one does. Despite the much larger amplitude the modes corresponding to the first resonance

yield a peak intensity which is smaller than those of the second and third resonances. For higher order acoustic resonances, the same explanation accounts for the alternating weak and medium peak intensities. Because of the $m\pi/2e$ shift in $\Delta>0$ acoustic resonances, the relative positions between acoustic resonances and maxima in the $\Delta=0$ spectrum yield a monotonic decay of peak intensity. The filtering of the $\Delta=0$ spectrum by the acoustic resonances becomes less and less effective when $|\Delta|\to 0$.

With respect to the maxima in spectrum $\Delta=0$, acoustic resonances are at lower (higher) wave numbers for $\Delta>0$ (<0): consequently, the peak positions shift progressively downward (upward) when $|\Delta|$ increases. This accounts for the observed continuous shifts of peak positions versus acoustic mismatch in contrast to the acoustic resonances [see Fig. 7(d)] and the observed asymmetric peak shapes [peaks display tails on the high (low) frequency side for $\Delta>0$ (<0)].

These numerical results show that there is a strong interplay between acoustic, photoelastic, and optical effects in the scattering efficiency. Having considered the acoustically matched layer (Fig. 6) prior to mismatched ones (Fig. 7), has allowed us to discriminate between their contributions. Unlike for a membrane, the peak positions are not determined solely by acoustics. Peak positions are not regularly spaced [Fig. 7(d)]. They are not simply related to frequencies of a set of discrete or confined modes. Moreover, we emphasize that acoustic mode confinement in the supported layer is not a prerequisite: Acoustic resonances are not even required to obtain a modulation in the scattered intensity (i.e., see $\Delta=0$). Assigning each broad peak in the spectrum to a given single mode is not a suitable interpretation since the spectrum involves a continuum of acoustic modes.

B. SOI structures

1. BOX-layer effects

Prior to considering a Si/SiO_2 bilayer on a silicon substrate, we point out that acoustic mismatch is negative ($\Delta=-0.33$) for a silicon layer on a silicon oxide substrate. The acoustic resonances are broad [Fig. 7(a)] and the scattering efficiency displays rather broad peaks too [Fig. 7(c)]. Furthermore, the peak width is about five times larger than the spectral resolution. In actual SOI structures, one has to consider additional acoustic and optical boundary conditions due to the SiO_2/Si substrate interface. In this section, we especially focus on the dependence of the ILS on the Buried OXide (BOX) layer-related acoustic and optical cavity effects by varying e_{BOX}, while keeping e constant.

The vibrational amplitude in the SOI layer oscillates as a function of wave number (Fig. 8), with two characteristic periods. One is related to the SOI-layer acoustic resonances, another to the BOX-layer ones; they scale inversely with e and e_{BOX}, respectively. When e and e_{BOX} are comparable (see $e=30$ nm and $e_{BOX}=35$ nm in Fig. 8), characteristic beats are observed. For thicker SiO_2 layers, one can easily identify the SOI- and BOX-related periods. Notice that, due to the relatively small acoustic mismatch between Si and SiO_2, the

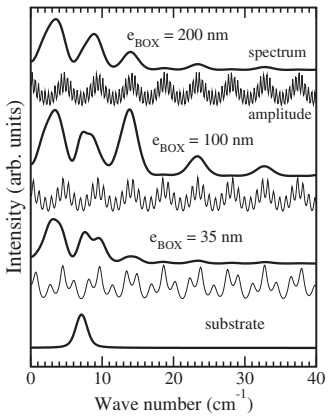

FIG. 8. Calculated spectra of SOI structures with $e=30$ nm and $e_{BOX}=35$, 100, and 200 nm (RT, $\lambda_i=413.1$ nm and $\Gamma=1.4$ cm^{-1}). The resonances of the acoustic mode amplitudes are also reported. The $1/\sqrt{\omega}$ term related to the mode normalization is not included here, unlike in Fig. 7(a). The lowest curve displays the Brillouin peak originating from the Si substrate.

oscillations are actually superimposed on a background of about three times the oscillation amplitude.

The cavity effects discussed already for the membrane and supported layer are also relevant here. Calculated spectra reported in Figs. 7 and 8 look similar. The Si substrate contributes to the spectra. The spectrum calculated for a bare Si substrate is also shown for comparison. It displays a single peak, the Brillouin peak of a very thick layer (Fig. 4). We present calculations including a $\Gamma=1.2$ cm^{-1} broadening, which is about the spectral resolution available in our experiments. Figure 8 shows that this broadening does not allow one to resolve the intensity modulation related to the BOX acoustic resonances. Nevertheless, the ILS spectra depend significantly on e_{BOX}. The peak intensities undergo striking changes when varying e_{BOX} while peak positions almost do not change. Notice the strong intensity of the third peak for $e_{BOX}=100$ nm. Above 15 cm^{-1}, the intensity ratio between successive odd and even SOI layer-related acoustic resonances depends strongly on e_{BOX}. With respect to the acoustic resonances, there is an apparent alternate quasiabsence of scattering for thick BOX layers. As for membranes (Fig. 3) and the supported layers (Fig. 7), the even acoustic resonances yield weak contributions. As the structures have the same e and the same $p(z)$ profile within the Si layer, this is a pure BOX-related optical cavity effect. The optical cavity effects may provide (i) a global enhancement of the scattered intensity and/or (ii) more selective enhancement of given acoustic resonances. The spatial dependence of $P_{pe}(z,t)$ contributes to the selective enhancement. The detailed investigation of the SiO_2-layer-related optical cavity effects is beyond the scope of the present paper. The corresponding resonances are expected to occur for specific e_{BOX} values (see Fig. 8) and to deal with the incident field and/or the scattered ones. Selective enhancement of Raman signals was reported for semiconductor planar microcavities.[31,32,34] For low-finesse microcavities (e.g., a single layer grown on a distributed Bragg reflector), it was shown that one can account for the experimental data by considering separately the enhance-

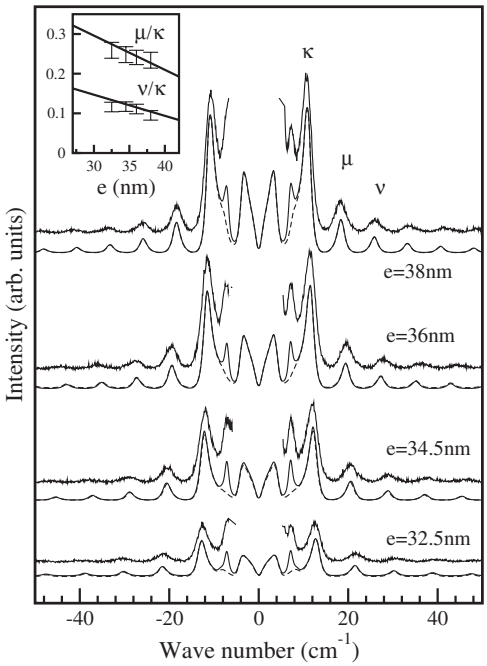

FIG. 9. Experimental BS spectra of SOI structures $e=32.5$, 34.5, 36, and 38 nm (RT, $\lambda_i=413.1$ nm and $\Gamma=1.5$ cm^{-1}) and calculated spectra (solid lines). Dashed lines are spectra calculated disregarding the Si substrate contribution. Inset: experimental and calculated intensity ratios (symbols and lines, respectively) versus e, where μ/κ and ν/κ refer to the peak labels.

ments of the incident field and the emission. Scattering efficiencies were obtained by calculating electric fields at the site of emitting dipoles in the presence of the cavity.[32] Note that, in contrast with our calculations, spatial averaging of the scattering efficiency through the structure had to be performed in order to enable comparison with experiment.[34] The separate presence of both excitation and emission enhancements were probed by performing experiments with different incidence angles and spectral features.[32,34] In our case, we varied e_{BOX} in the calculations. The corresponding changes in the optical cavity clearly modify the scattering efficiencies for the different acoustic resonances (Fig. 8).

To summarize this part, relative peak intensities in a SOI spectrum depend on the $p(z)$ profile, the optical cavity, and induced interferences. Calculating spectra is thus a matter of fulfilling electromagnetic boundary conditions in the presence of $P_{pe}(z,t)$. Since optical cavity effects play a major role in the ILS from SOI, one needs to go beyond the simple scheme involving electromagnetic modes calculated in the absence of $P_{pe}(z,t)$.

2. Comparison with experiment

Figure 9 shows both experimental and calculated SOI spectra. They compare rather well. Data reported in Fig. 9 correspond to different SOI-layer thicknesses, the BOX thickness being the same $e_{BOX}=400$ nm. Spectra display peaks related to a continuum of LA modes, which are significantly broader than the experimental spectral resolution. This assignment differs obviously from the one given in Ref. 21 where peaks were attributed to a given finite set of confined shear acoustic modes, by comparing experimental peak frequencies to calculated ones. Moreover, the spectral range, which appears to be of particular relevance according to the results presented here, was not investigated in Ref. 21; only data above ≈ 50 cm^{-1} was presented.

The scattering efficiencies in Fig. 9 depend strongly on the acoustic and electromagnetic boundary conditions. In SOI structures, all interfaces, including the oxide/substrate one, have to be considered. When increasing e, the peak spacing within each spectrum decreases slowly, as expected. Calculations compare rather well to the experimental data. Due to the thick BOX layer ($e_{BOX}=400$ nm), acoustical resonances in the SOI layers only contribute alternatively to the scattering above 15 cm^{-1} (see Fig. 8). Similar alternate contributions were reported for supported silicon oxynitride films[12] and ZnSe films on GaAs.[13] There are some discrepancies at high wave numbers, typically above 30 cm^{-1}. The calculations overestimate slightly the peak intensities and do not account for the observed peak asymmetry (peaks display a tail on their high frequency side). According to the optical cavity effects pointed out above, the peak intensities depend strongly on e. Evaluating intensity ratios is a relevant test for the calculations. The inset in Fig. 9 shows the intensity ratios between the peaks labeled κ, μ, and ν.

In order to identify the substrate contribution to the spectra, calculations were also performed assuming no photoelastic contribution in the substrate (dashed lines in Fig. 9). This allows one to clearly identify the Brillouin contribution of the substrate. The intensity ratio between this Brillouin peak and the strongest one (labeled κ) originating from the Si layer changes substantially when e varies from $e=32.5-38$ nm; this is again a signature of the optical cavity effects. Although the intense Rayleigh scattering hinders the quantitative comparison between experiment and calculations in this low frequency range, the calculations apparently account for the observed trends. The number of parameters was kept to a minimum in the calculations and a global satisfactory agreement between calculations and experiment was obtained.

VI. DISCUSSION AND CONCLUSION

Experimental spectra of a membrane and supported layer look rather similar at first sight. Following the progressive analysis presented above, one is able to understand these similarities and at the same time point out differences in the underlying physics. A major difference to be emphasized is that for the membrane only a discrete set of confined modes is available, whereas for the supported layer one deals with a continuum of modes. Furthermore, the experimentally observed peak width is given by the experimental spectral resolution for the membrane and it is basically intrinsic for the supported layer. For both membranes and supported layers, the spectral response results from a strong interplay between acoustic, optical, and photoelastic effects. Within the frame of the model adopted here, they are included in the polarization $P_{pe}(z,t)$ [see Eq. (1)]. The way scattered light gets out of the structure is definitely a matter of satisfying acoustic and

optical boundary conditions (Fig. 2). It was shown that optical cavity effects play a specific role for thin layers (see Fig. 4). The photoelastic model adopted here [Eq. (3), the wave equation including $P_{pe}(z,t)$] accounts rather well for the experimental data, including peak positions, widths, and intensities. The spatial localization of the photoelastic coupling, introduced when choosing the $p(z)$ profile, determines the envelope of the spectral response (see Fig. 1). Unlike in previous reports on thicker layers,[12,13,16] here the strongest contributions arise from the three first order confined modes or acoustic resonances.

In a very recent theoretical paper, photoelastic model ILS calculations (based on the integral version [Eq. (2)]) and quantum model ones were compared for thin Si membranes.[30] The dependence on optical excitation in the vicinity of the direct transition at 4.2 eV was investigated. For resonant excitation, quantum model calculations are required. Out of resonance (below the transition), both models may yield similar spectra, depending on $p(z)$. It was suggested that a trapezoidal-like profile would be more realistic than a step-like one, for $e<25$ nm. However, the optical cavity effects were, however, not considered in Ref. 30, neither in the photoelastic model nor in the quantum model. Only odd modes were predicted to contribute to the ILS from membranes,[30] in contrast with experimental findings for BS.[20] Our study shows that, independently of the details of the $p(z)$ profile, disregarding optical cavity effects is not satisfactory to simulate ILS spectra of thin Si membranes. Seeking for finite size effects on $p(z)$ is definitely a stimulating issue, for both Si membranes and supported layers. Following Ref. 30, investigating the dependence on λ_i would be particularly relevant. The excitation energy we used here is about 1 eV below the one considered in Ref. 30; it does not fit with a particular electronic transition. Contributions of many electronic states are thus expected. Therefore a rather uniform $p(z)$ profile in the Si layer is likely to provide a satisfactory description for the photoelastic coupling.

Before going into more detail in the simulations, one should also evaluate quantitatively the effects of thin surface oxide layers (which yield additional cavities) and finite collection angles (which enable modes with nonzero in-plane wave vectors to contribute). For the sake of simplicity, these effects were not included in the calculations presented here. Doing so, we were able to track the contributions of the main cavity effects discussed above. Here we focused on a simple geometrical configuration, FS and BS along the z axis. The angular dependence of the ILS in thin Si layers has to be investigated as well. Analyzing ILS by acoustic modes having finite in-plane wave vectors would require:

(i) A better spectral resolution and an improved signal to noise ratio at high wave numbers.

(ii) To include the ripple coupling in the calculations.

The contributions of photoelastic and ripple coupling mechanisms, as well as their possible interferences, have to be calculated.[3,4,7,13] This could be performed in the frame of the present model, following previous Brillouin scattering studies.[4] Noteworthy, ripple mechanisms were also considered in quantum models for semiconductor QDs[46] and metallic QDs.[47]

The study of acoustic modes having finite in-plane wave vectors, and their interaction with electrons in the Si layers is a crucial issue with respect to applications, in particular, to carrier and heat transport. The corresponding elastic properties underlie many nanoelectromechanical applications. ILS provides a powerful means for probing acoustic properties and electron-phonon interaction in thin Si layers. The present study clearly shows that in order to derive quantitative information from the experimental data, optical and photoelastic cavity effects have to be taken into account in the calculations. As shown in Fig. 7, for a given layer thickness the acoustic resonance frequencies may differ from the peak positions in the ILS spectra. Directly assigning experimental peak frequencies to calculated acoustic resonance frequencies may therefore cause significant errors in the evaluation of elastic properties. For instance, errors on derived sound velocities could be as high as 5%.

To summarize, ILS by LA acoustic modes in thin Si membranes and supported layers has been investigated. Calculations performed within the frame of the photoelastic model were presented. It was shown that the scattering efficiency results from a strong interplay between acoustic, optical, and photoelastic cavity effects. Their respective contributions to the scattering efficiency were identified. Optical cavity effects were found to play a major role. Electromagnetic fields are stationary inside the Si layers and include a phonon-related spatial dependence. The wave equation has to be solved in the presence of the polarization $P_{pe}(z,t)$ induced by the photoelastic effect. This allows one to include simultaneously the acoustic and optical boundary effects when calculating the scattering efficiency. Calculations and experimental data were successfully compared for Si membranes and SOI structures. Whereas the spectra of the former involve a discrete set of confined modes, the spectra of the latter involve a continuum of acoustic modes. The thin supported and unsupported layers considered here are particularly interesting as model systems to investigate ILS from single objects. We conclude that a comprehensive comparison between theory and experiment is of significance not only for identifying the relevant modeling and coupling mechanisms but also for future studies aiming to characterize elastic properties and/or to probe electron-phonon interaction in thin Si layers.

ACKNOWLEDGMENTS

C.M.S.T. gratefully acknowledges support from the University Paul Sabatier and the CNRS. M.P. and J.A. acknowledge the support of the EU project No. IST-2001-38937 EXTRA and the Academy of Finland project No. 205467 CODE. This work was partly supported by the Science Foundation of Ireland (Grant No. 02/IN.1/172). J.A. and C.M.S.T. thank the partial support of the EC-funded project PHOREMOST (FP6/2003/IST/2-511616). The content of this work is the sole responsibility of the authors.

*jesse.groenen@cemes.fr

[1] N. L. Rowell and G. I. Stegeman, Phys. Rev. Lett. **41**, 970 (1978).
[2] V. Bortolani, F. Nizzoli, G. Santoro, A. Marvin, and J. R. Sandercock, Phys. Rev. Lett. **43**, 224 (1979).
[3] V. Bortolani, F. Nizzoli, G. Santoro, and J. R. Sandercock, Phys. Rev. B **25**, 3442 (1982).
[4] V. Bortolani, A. M. Marvin, F. Nizzoli, and G. Santoro, J. Phys. C **16**, 1757 (1983).
[5] M. Grimsditch, R. Bhadra, and I. K. Schuller, Phys. Rev. Lett. **58**, 1216 (1987).
[6] B. Hillebrands, S. Lee, G. I. Stegeman, H. Cheng, J. E. Potts, and F. Nizzoli, Phys. Rev. Lett. **60**, 832 (1988).
[7] J. M. Karanikas, R. Sooryakumar, and J. M. Phillips, Phys. Rev. B **39**, 1388 (1989).
[8] F. Nizzoli, C. Byloos, L. Giovannini, C. E. Bottani, G. Ghislotti, and P. Mutti, Phys. Rev. B **50**, 2027 (1994).
[9] G. Ghislotti and C. E. Bottani, Phys. Rev. B **50**, 12131 (1994).
[10] G. Ghislotti, C. E. Bottani, P. Mutti, C. Byloos, L. Giovannini, and F. Nizzoli, Phys. Rev. B **51**, 9875 (1995).
[11] X. Zhang, M. H. Manghnani, and A. G. Every, Phys. Rev. B **62**, R2271 (2000).
[12] X. Zhang, R. Sooryakumar, A. G. Every, and M. H. Manghnani, Phys. Rev. B **64**, 081402(R) (2001).
[13] X. Zhang, R. S. Bandhu, R. Sooryakumar, and B. T. Jonker, Phys. Rev. B **67**, 075407 (2003).
[14] X. Zhang, R. Sooryakumar, and K. Bussmann, Phys. Rev. B **68**, 115430 (2003).
[15] R. S. Bandhu, X. Zhang, R. Sooryakumar, and K. Bussmann, Phys. Rev. B **70**, 075409 (2004).
[16] J. R. Sandercock, Phys. Rev. Lett. **29**, 1735 (1972).
[17] R. Loudon, Phys. Rev. Lett. **40**, 581 (1978).
[18] N. L. Rowell and G. I. Stegeman, Phys. Rev. B **18**, 2598 (1978).
[19] C. Byloos, L. Giovannini, and F. Nizzoli, Phys. Rev. B **51**, 9867 (1995).
[20] C. M. Sotomayor Torres, A. Zwick, F. Poinsotte, J. Groenen, M. Prunnila, J. Ahopelto, A. Mlayah, and V. Paillard, Phys. Status Solidi C **1**, 2609 (2004).
[21] A. Balandin, Phys. Low-Dimens. Semicond. Struct. **5**, 73 (2000).
[22] C. Colvard, T. A. Gant, M. V. Klein, R. Merlin, R. Fischer, H. Morkoc, and A. C. Gossard, Phys. Rev. B **31**, 2080 (1985).
[23] A. Fainstein and B. Jusserand, in *Light Scattering in Solids IX*, edited by M. Cardona and R. Merlin (Springer-Verlag, Berlin, Heidelberg, 2007).
[24] P. X. Zhang, D. J. Lockwood, and J.-M. Baribeau, Can. J. Phys. **70**, 843 (1992).
[25] M. W. C. Dharma-wardana, P. X. Zhang, and D. J. Lockwood, Phys. Rev. B **48**, 11960 (1993).
[26] O. Pilla, V. Lemos, and M. Montagna, Phys. Rev. B **50**, 11845 (1994).
[27] M. Trigo, A. Fainstein, B. Jusserand, and V. Thierry-Mieg, Phys. Rev. B **66**, 125311 (2002).
[28] M. Giehler, T. Ruf, M. Cardona, and K. Ploog, Phys. Rev. B **55**, 7124 (1997).
[29] M. Trigo, A. Bruchhausen, A. Fainstein, B. Jusserand, and V. Thierry-Mieg, Phys. Rev. Lett. **89**, 227402 (2002).
[30] A. Mlayah, J.-R. Huntzinger, and N. Large, Phys. Rev. B **75**, 245303 (2007).
[31] A. Fainstein, B. Jusserand, and V. Thierry-Mieg, Phys. Rev. Lett. **75**, 3764 (1995).
[32] A. Fainstein, B. Jusserand, and V. Thierry-Mieg, Phys. Rev. B **53**, R13287 (1996).
[33] A. Fainstein and B. Jusserand, Phys. Rev. B **54**, 11505 (1996).
[34] A. Fainstein and B. Jusserand, Phys. Rev. B **57**, 2402 (1998).
[35] T. Ruf, in *Phonon Raman Scattering in Semiconductors, Quantum Wells and Superlattices*, Vol. 142 of Springer Tracts in Modern Physics, edited by G. Hohler (Springer-Verlag, Berlin, 1998).
[36] M. Bruel, B. Aspar, and A. J. Auberton-Herve, Jpn. J. Appl. Phys., Part 1 **36**, 1636 (1997).
[37] C. Trallero-Giner, F. Comas, and F. García-Moliner, Phys. Rev. B **50**, 1755 (1994).
[38] W. Hayes and R. Loudon, *Scattering of Light by Crystals* (Wiley, New York, 1978).
[39] J. He, B. Djafari-Rouhani, and J. Sapriel, Phys. Rev. B **37**, 4086 (1988).
[40] *Semiconductors: Group IV and III–V Compounds*, edited by O. Madelung (Springer-Verlag, Berlin, 1991).
[41] D. E. Aspnes and A. A. Studna, Phys. Rev. B **27**, 985 (1983).
[42] I. H. Malitson, J. Opt. Soc. Am. **55**, 1205 (1965).
[43] P. Etchegoin, J. Kircher, and M. Cardona, Phys. Rev. B **47**, 10292 (1993).
[44] If one considers a thick but finite substrate, quantization of q_z wave vectors occurs. For large total thickness, this quantization would, however, result in a quasicontinuum of acoustic modes.
[45] B. Jusserand, F. Alexandre, J. Dubard, and D. Paquet, Phys. Rev. B **33**, 2897 (1986).
[46] P. A. Knipp and T. L. Reinecke, Phys. Rev. B **52**, 5923 (1995).
[47] G. Bachelier and A. Mlayah, Phys. Rev. B **69**, 205408 (2004).